Stem Cell Reports
Article

OPEN ACCESS

Defective *Tmprss3*-Associated Hair Cell Degeneration in Inner Ear Organoids

Pei-Ciao Tang,[1] Alpha L. Alex,[1] Jing Nie,[1] Jiyoon Lee,[1] Adam A. Roth,[1] Kevin T. Booth,[3] Karl R. Koehler,[1] Eri Hashino,[1,2] and Rick F. Nelson[1,*]

[1]Department of Otolaryngology-Head and Neck Surgery, Indiana University School of Medicine, Indianapolis, IN, USA
[2]Stark Neurosciences Research Institute, Indiana University School of Medicine, Indianapolis, IN, USA
[3]Molecular Otolaryngology and Renal Research Laboratories, Department of Otolaryngology, University of Iowa, Iowa City, IA, USA
*Correspondence: ricnelso@iupui.edu
https://doi.org/10.1016/j.stemcr.2019.05.014

SUMMARY

Mutations in the gene encoding the type II transmembrane protease 3 (*TMPRSS3*) cause human hearing loss, although the underlying mechanisms that result in *TMPRSS3*-related hearing loss are still unclear. We combined the use of stem cell-derived inner ear organoids with single-cell RNA sequencing to investigate the role of TMPRSS3. Defective *Tmprss3* leads to hair cell apoptosis without altering the development of hair cells and the formation of the mechanotransduction apparatus. Prior to degeneration, *Tmprss3*-KO hair cells demonstrate reduced numbers of BK channels and lower expressions of genes encoding calcium ion-binding proteins, suggesting a disruption in intracellular homeostasis. A proteolytically active TMPRSS3 was detected on cell membranes in addition to ER of cells in inner ear organoids. Our *in vitro* model recapitulated salient features of genetically associated inner ear abnormalities and will serve as a powerful tool for studying inner ear disorders.

INTRODUCTION

Auditory and vestibular systems share numerous molecular constituents, as well as a common molecular evolution, although these systems differ in their structure, cellular components, and physiological properties (Fritzsch and Straka, 2014; Gillespie and Muller, 2009). Defects in the conserved features may consequently impair both hearing and balance (Keats and Corey, 1999; Shinjo et al., 2007; Zhou et al., 2009). One such family of molecules includes type II transmembrane serine proteases, which are classified by their N-terminal anchor to membranes and contain an active C-terminal serine protease domain (Barre et al., 2014; Szabo and Bugge, 2011). One such type II transmembrane serine protease, TMPRSS3, is required for proper mammalian hearing, and mutations in *TMPRSS3* cause congenital and early-onset hearing loss (Scott et al., 2001). Indeed, large-scale sequencing projects investigating the genetic etiology of deafness revealed that ~9% of genetic-associated hearing loss cases are due to mutations in *TMPRSS3* (Bademci et al., 2016; Sloan-Heggen et al., 2016).

Our current understanding of the role of TMPRSS3 in the pathobiology of deafness comes from studies on mice harboring a nonsense mutation in *Tmprss3* (*Tmprss3*^{Y260X}), which results in a truncated protease domain (Fasquelle et al., 2011). These mice display normal cochlear and vestibular hair cells (HCs) in the early postnatal period followed by rapid cochlear HC degeneration starting on postnatal day 12 (P12) (Fasquelle et al., 2011). In addition, *Tmprss3* mutant mice display saccular abnormalities as well as aberrant vestibular function (Fasquelle et al., 2011). Despite these observations, the cellular function of TMPRSS3 and the mechanisms underlying HC degeneration have yet to be elucidated.

Previously, TMPRSS3 was implicated in regulating both epithelial sodium channels (ENaC [Guipponi et al., 2002]) and potassium calcium-activated channel subfamily M alpha 1 (KCNMA1 [Molina et al., 2013]). However, pseudohypoaldosteronism type I patients with defective ENaC in the cochlea have normal hearing (Peters et al., 2006). This suggests that while TMPRSS3 might contribute to ENaC regulation, TMPRSS3-mediated ENaC dysfunction is not the primary mechanism underlying auditory and vestibular dysfunction.

In recent years, organoid cultures have gained acceptance as *in vitro* models of various organ systems. They offer the advantages of scalability, accessibility, and the capacity for rapid and precise genetic manipulation in the laboratory. To better understand the defective *Tmprss3*-implicated HC degeneration, we capitalized on the stem cell-derived three-dimensional inner ear organoid system (Koehler et al., 2013; Liu et al., 2016), which features HCs characterized by the same structural and functional properties of vestibular HCs. Upon using this system, *Tmprss3* mutations resulted in HC apoptosis in both mouse vestibular sensory epithelia (*in vivo*) and inner ear organoids (*in vitro*); such congruency signifies that stem cell-derived inner ear organoids can recapitulate gene mutation-associated pathological features *in vivo*. The level of HC degeneration was dependent on the nature of the mutation (and consequently the structure of the resulting TMPRSS3 protein). Furthermore, we also revealed a previously undocumented subcellular localization of TMPRSS3. In combination with single-cell RNA sequencing (scRNA-seq) data, we propose

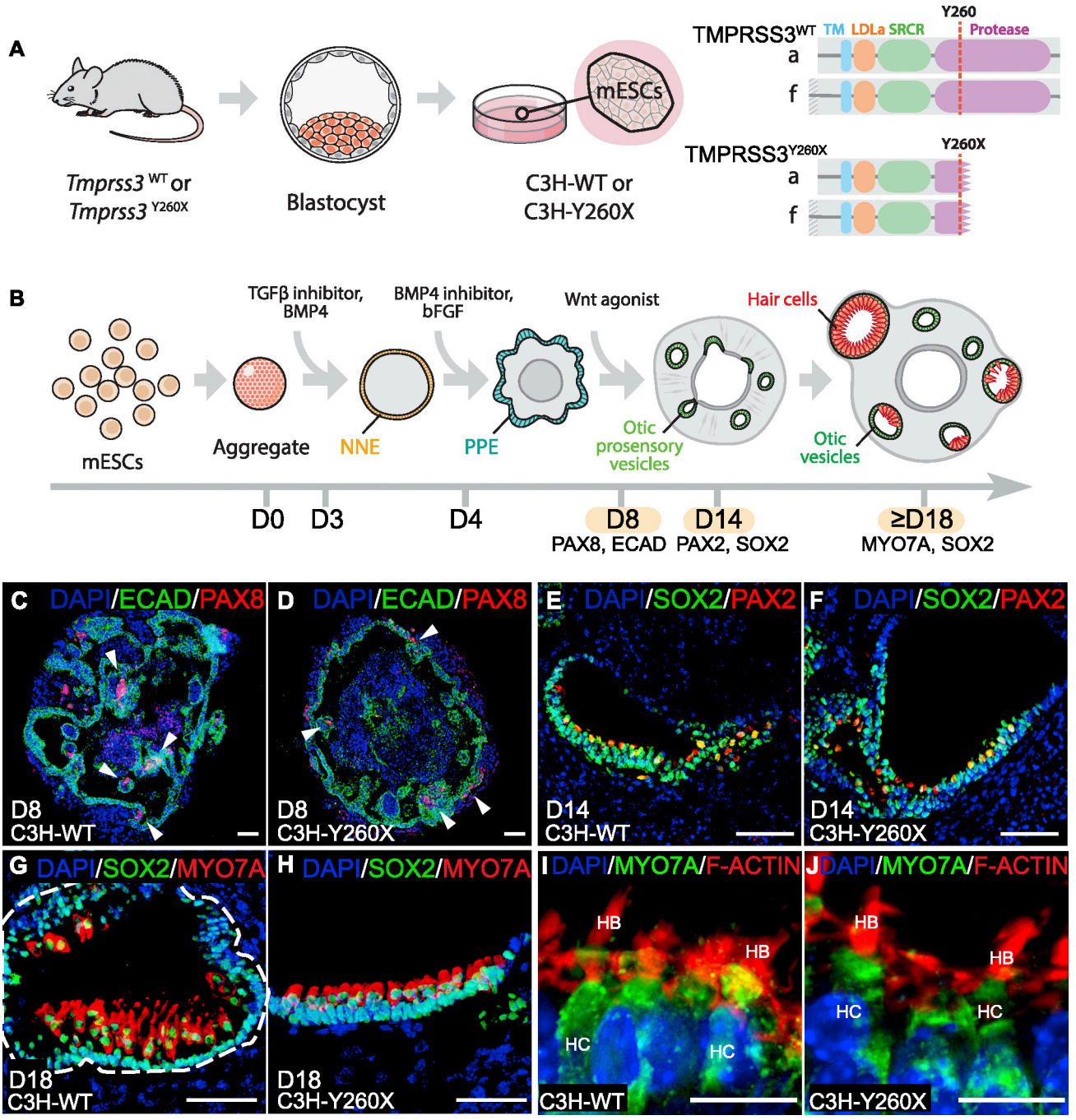

Figure 1. Normal Development and Formation of Hair Cells in Both Wild-Type and *Tmprss3* Mutant Inner Ear Organoids

(A) Schematic diagram of the derivation of mouse embryonic stem cells (mESCs) from wild-type (WT) (*Tmprss3*^{WT}) and *Tmprss3*^{Y260X} mice. TMPRSS3 protein domains are shown for both WT and Y260X mutants.

(B) Schematic diagram of the induction of inner ear organoids from mESCs. Three major time points (day 8 [D8], D14, and ≥D18) for checking the development of inner ear organoids are denoted by key molecular markers.

(C and D) Representative images of ECAD and PAX8 staining in D8 aggregates. White arrowheads indicate the ECAD^{+}PAX8^{+} otic-epibranchial placode domain.

(E and F) SOX2^{+} and PAX2^{+} otic prosensory vesicles in D14 aggregates.

(G and H) Otic vesicles in D18 aggregates. MYO7A^{+} hair cells (HC) and SOX2^{+} supporting cells are also evident. White dashed lines encircle the sensory epithelium.

(legend continued on next page)

several potential roles of TMPRSS3 in HC degeneration. These findings highlight the unique advantages in using organoid systems to model disease mechanisms and have improved our understanding of the role of TMPRSS3 in the inner ear.

RESULTS

TMPRSS3 Protease Activity Is Not Required for Proper Inner Ear Organoid Development

To establish the stem cell-derived inner ear organoid model of *Tmprss3* dysfunction, we began by comparing the pathological effects of *Tmprss3* mutations in HCs between a previously generated mouse model (Fasquelle et al., 2011) and inner ear organoids. *Tmprss3* mutant mice ($Tmprss3^{Y260X}$) carrying a nonsense mutation, which results in a truncated protease domain (Figure 1A), were used as the *in vivo* counterparts. We derived mouse embryonic stem cell (mESC) lines from both wild-type (WT; $Tmprss3^{WT}$) and mutant $Tmprss3^{Y260X}$ mice on the same C3HeB/FeJ background strain (Figure 1A). After characterization, we selected a WT (C3H-WT) and a mutant (C3H-Y260X) cell line, and the pluripotency of these mESC lines were verified using three pluripotency markers: OCT3/4, NANOG, and SOX2 (Figure S1).

Inner ear organoids were derived from both C3H-WT and C3H-Y260X, and the development of organoids was checked with specific molecular markers at three key time points (Figure 1B) based on the previous study by Koehler et al. (2013). Both C3H-WT and C3H-Y260X ESC lines generated $PAX8^+ECAD^+$ otic-epibranchial placode domains (OEPD) on culture day 8 (D8) (Figures 1C and 1D), followed by $PAX2^+SOX2^+$ otic prosensory vesicles on D14 (Figures 1E and 1F). On D18, otic vesicles containing $MYO7A^+$ HCs and $SOX2^+$ supporting cells (SCs) were observed in both C3H-WT and C3H-Y260X organoids (Figures 1G and 1H). Hair bundles (HBs), unique structures composed of ACTIN-based stereocilia, were visible in both C3H-WT and C3H-Y260X HCs (Figures 1I and 1J). These initial assessments confirmed that the mESCs derived in this study produced inner ear organoids comparable with those of previous studies and were suitable for downstream analyses. Moreover, these results imply that the truncated TMPRSS3 affected neither the development of inner ear organoids nor the formation of HCs.

TMPRSS3 Proteins with Truncated Protease Domains Result in Elevated Apoptotic Signals in Inner Ear Hair Cells *In Vivo* and *In Vitro*

A previous study demonstrated rapid degeneration in cochlear HCs between P12 and P14 in $Tmprss3^{Y260X}$ mice (Fasquelle et al., 2011). According to electrophysiological data, organoid HCs showed developmental patterns (with respect to timing and physiology) similar to those of mice, and HCs on culture days 22–27 demonstrated comparable mechanosensitivity to P2–P5 mouse utricle HCs (Liu et al., 2016). In this study we extended the culture period to 40 days, which allowed for the growth of HCs that were equivalent to those of P12–P14 mice. We analyzed the sensory epithelia for signs of HC degeneration both *in vivo* and *in vitro*. Consistent with the previous study (Fasquelle et al., 2011), we observed the loss of HCs in $Tmprss3^{Y260X}$ cochlea by P14 (Figure S2). Even though the loss of HCs in vestibular organs was not as prominent as in the cochlea, significantly elevated signals of the apoptosis marker cleaved CASPASE 3 (CASP3) were detected in the sensory epithelia of utricles and saccules of $Tmprss3^{Y260X}$ relative to those of $Tmprss3^{WT}$ on P14 ($p < 0.05$; Figures 2A–2F). Although there were higher CASP3 levels in the crista of $Tmprss3^{Y260X}$ versus those of $Tmprss3^{WT}$ (Figures 2G–2I), this difference was not statistically significant.

Next, we examined mESC-derived organoids from these mice for signs of apoptosis and HC degeneration. Otic vesicles in both C3H-WT and C3H-Y260X organoids on D28 and D33 were characterized by indistinguishable levels of CASP3 (Figure S3). However, by D38, significantly elevated CASP3 levels were detected in the sensory epithelia of C3H-Y260X versus C3H-WT ($p < 0.05$; Figures 2J–2L). A similar level of increase in CASP3 (~45%) was measured in otic vesicles and in mouse sensory epithelia (Figure 2). In summary, defective TMPRSS3 with truncated protease domains lead to elevated apoptotic signals in sensory epithelia in both mouse and inner ear organoids at similar stages (P14 versus D38, respectively).

Tmprss3 Knockout Inner Ear Organoids Undergo Normal Early Development

In humans, different mutations in *TMPRSS3* lead to variable phenotypes (Lee et al., 2003; Weegerink et al., 2011). We sought to determine the effect of complete loss of

(I and J) Representative images of $MYO7A^+$ HCs with F-ACTIN-based hair bundles (HB) in D25 organoids.
(C) to (J) show otic vesicles (n = 15) from three independent experiments. Other abbreviations: TM, transmembrane; LDLa, low-density lipoprotein a; SRCR, scavenger receptor cysteine-rich; NNE, non-neural ectoderm; PPE, pre-placodal ectoderm; TGFβ, transforming growth factor β; BMP4, bone morphogenetic protein 4; FGF, fibroblast growth factor . Scale bars, 50 μm (C–H) and 10 μm (I and J). See also Figures S1 and S7.

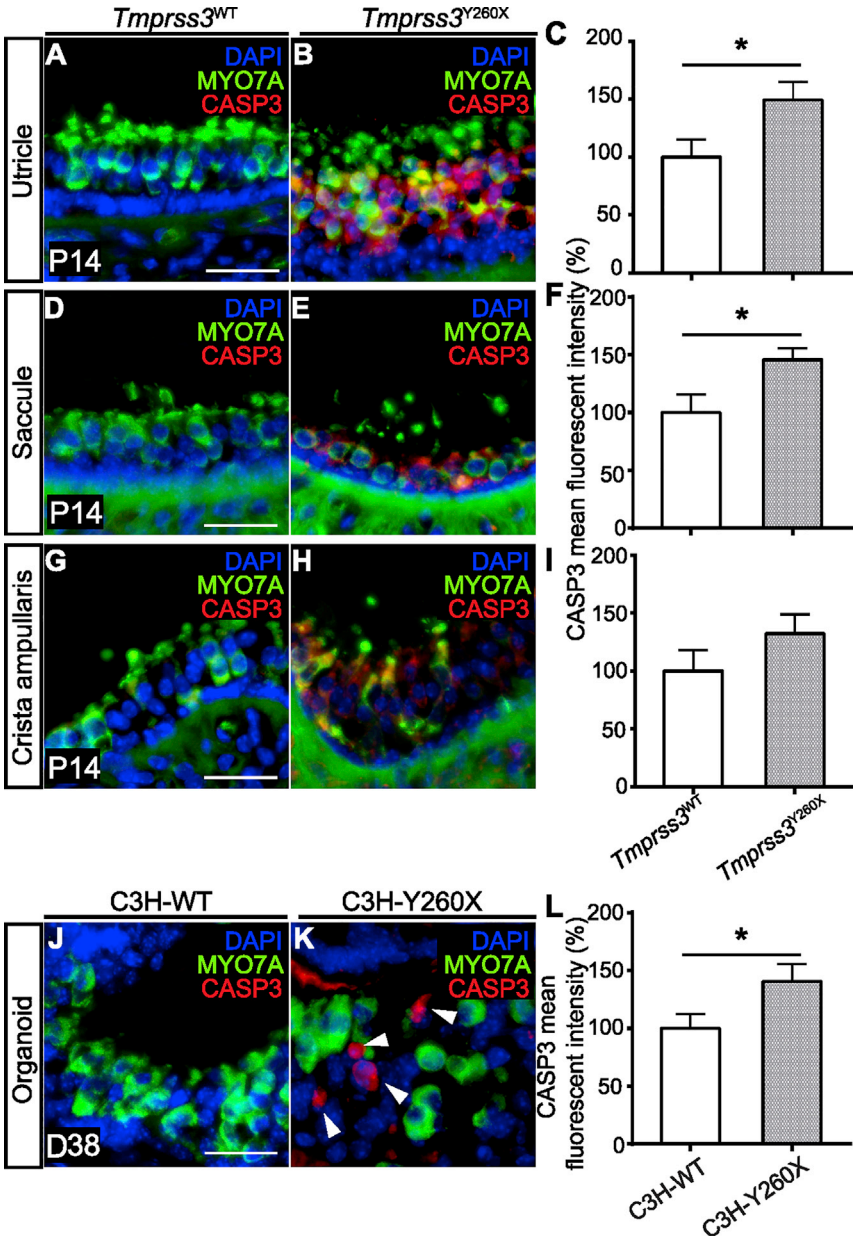

Figure 2. Increase in Signals of the Apoptotic Marker Cleaved CASPASE-3 in Inner Ear Sensory Epithelia (Both *In Vivo* and *In Vitro*) with *Tmprss3* Mutations

(A–I) Representative images of mouse utricle (A and B), saccule (D and E), and crista ampullaris (G and H) from P14 *Tmprss3*^{WT} and *Tmprss3*^{Y260X} mice, respectively. Quantification of the percent of mean (±SEM; n = 6 sensory epithelia) cleaved caspase-3 (CASP3) fluorescence intensity in *Tmprss3*^{Y260X} relative to *Tmprss3*^{WT} for the utricle (C), saccule (F), and crista ampullaris (I).

(J and K) Representative images of D38 inner ear organoids as indicated, with MYO7A and CASP3 staining. White arrowheads indicate CASP3^{+} hair cells.

(L) Percent of mean (±SEM; n = 14 and 16 otic vesicles for C3H-WT and C3H-Y260X, respectively, from three independent experiments) CASP3 fluorescence intensity of otic vesicles in C3H-Y260X relative to C3H-WT.

For the quantitative data, raw images (without any image processing/modification) were analyzed with ImageJ (Student's t test, *p < 0.05). CASP3 fluorescence intensity of the WT condition was set arbitrarily at 100%. Scale bars, 25 μm. See also Figures S2 and S3.

TMPRSS3 on HC development and survival. Furthermore, due to the lack of a specific TMPRSS3 antibody, the presence and localization of TMPRSS3 among inner ear cell types is unclear. To eliminate TMPRSS3 synthesis and observe gene expression under the endogenous *Tmprss3* promoter, we generated a *Tmprss3*-knockout (KO)/nGFP-knockin cell line using the commercially available mESC line R1/E. By using this second ESC line, we sought to verify whether the phenomena associated with *Tmprss3* mutations are comparable across cell lines.

Previously, two *Tmprss3* transcript variants (a and f) were reported (Fasquelle et al., 2011). To knock out both transcripts and also create a *Tmprss3* reporter, we inserted a nuclearly localized GFP (2A-nGFP) cassette with a stop codon in-frame into exon 2 of *Tmprss3* (Figure 3A); this resulted in 2A-nGFP being transcribed by the endogenous *Tmprss3* promoter (Figure 3A). Correct biallelic insertion of the 2A-nGFP cassette in the mESC *Tmprss3* locus was confirmed by PCR and DNA sequencing (Figures 3B and 3C; Supplemental Information). No off-target indel was found based on DNA sequencing (Table S1), and the pluripotency of the modified mESCs (named "*Tmprss3*KO-GFPKI") was verified with pluripotency markers (Figures 3D–3F).

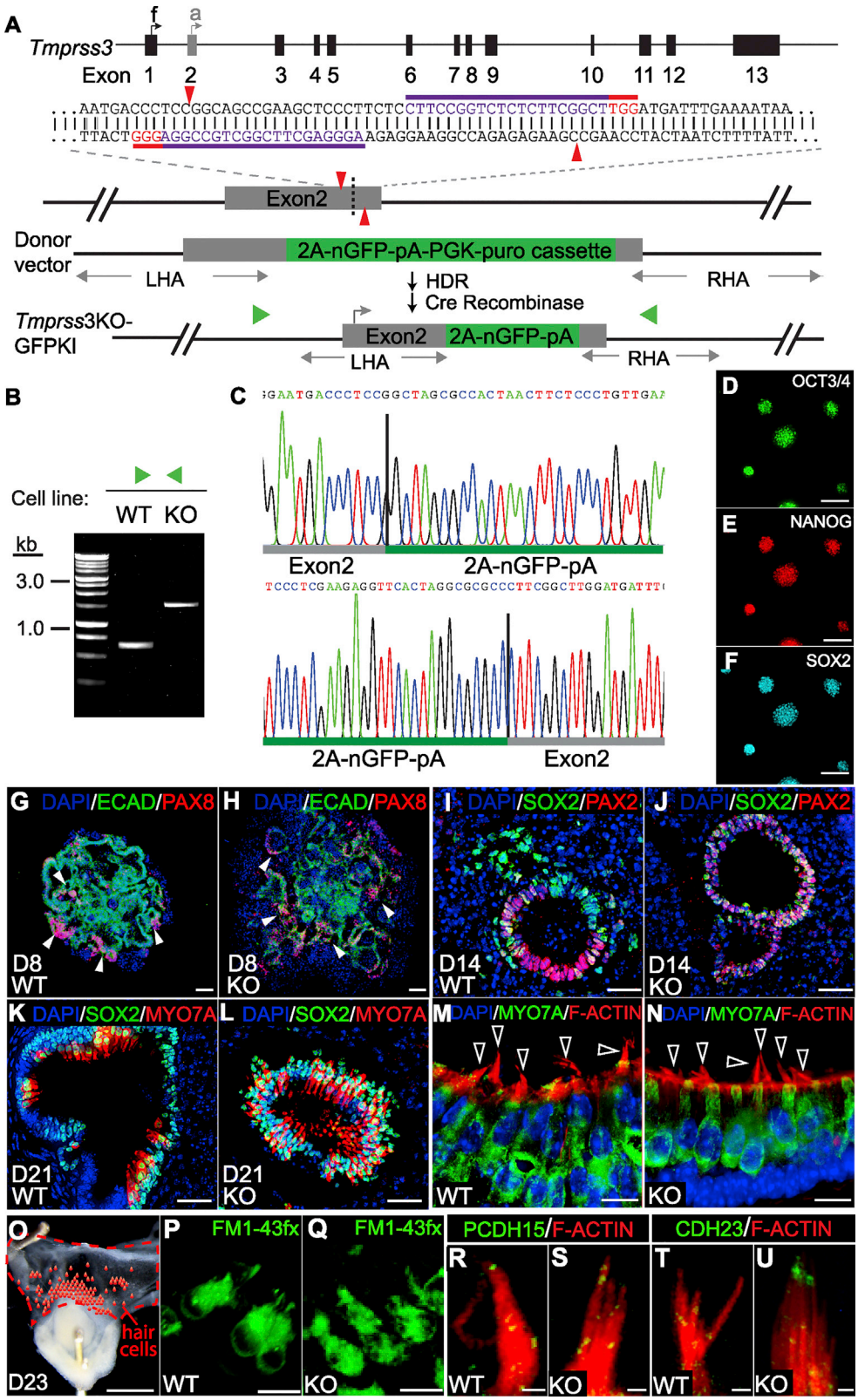

(legend on next page)

The early development of inner ear organoids in *Tmprss3*KO-GFPKI (KO) was examined at three key time points: D8, D14, and D21 (Figure 1B); R1/E (WT)-derived organoids served as controls. On D8, $PAX8^+ECAD^+$ OEPD was seen in both WT and KO aggregates (Figures 3G and 3H). By D14, aggregates contained $PAX2^+SOX2^+$ otic prosensory vesicles (Figures 3I and 3J) followed by presence of otic vesicles containing $MYO7A^+$ HCs with $SOX2^+$ SCs and F-ACTIN-based HBs in both WT and KO organoids on D21 (Figures 3K–3N). FM1-43fx uptake patterns suggested that HCs in both WT and KO (D23) otic vesicles possessed mechanotransduction channels (Figures 3O–3Q). Furthermore, protocadherin-15 (PCDH15; Kazmierczak et al., 2007) and cadherin-23 (CDH23; Siemens et al., 2004) antibodies (gifts from Dr. Ulrich Muller) labeled tip links of D23 HBs (Figures 3R–3U). These results signify that complete loss of TMPRSS3 alters neither the development of otic vesicles nor the formation of HCs (and their mechanotransduction apparatus) in inner ear organoids.

Degeneration of Hair Cells in D38 *Tmprss3*-KO Inner Ear Organoids

We next examined whether the loss of TMPRSS3 leads to HC degeneration. Along with GFP and CASP3 staining, HCs were labeled with the HC marker calretinin, and the structure of the sensory epithelia was examined by two conventional SC markers, SOX2 and SOX9 (Mak et al., 2009; Oesterle et al., 2008). On D28 and D33, the structure of the otic vesicles, the integrity of the HCs, and the lack of CASP3 labeling on HCs all pointed to an absence of HC degeneration in both R1/E (WT) and *Tmprss3*KO-GFPKI (KO) organoids (Figures 4A–D′, S4A, and S4B). However, by D38, HCs in KO organoids were disorganized and presented higher CASP3 signals relative to D38 WT organoids (Figures 4E–4F′, S4C, and S4D). Because disrupted otic vesicles were documented frequently in D38 KO organoids, such structural aberrancies hindered the measurement of CASP3 fluorescence intensity in sensory epithelia and led to highly variable labeling data. Therefore, western blots were used to quantify the difference in CASP3 levels between D36 WT and KO organoids (Figures 4G and 4H). A 3-fold increase in CASP3 levels (normalized to β-ACTIN concentrations) was detected in D36 KO organoids compared with D36 WT organoids ($p < 0.001$; Figure 4H).

We also investigated the effects of *Tmprss3*-KO between HCs and the surrounding SCs by comparing the percentage of $CASP3^+$ HCs and $CASP3^+$ SCs in D36 KO organoids (Figure 4I). A significant difference between the percentage of $CASP3^+$ HCs (12.3% ± 2.7% SEM) and $CASP3^+$ SCs (<0.01%) per otic vesicle was seen ($p < 0.001$), suggesting that *Tmprss3*-KO-associated degeneration occurs predominantly in HCs (and not other sensory epithelia cell types). Thus, we conclude that *Tmprss3*-KO leads to severe HC degeneration by D38 through an apoptosis pathway that occurs between D33 and D38.

Decreased Presence of BK Channels in *Tmprss3*-KO Hair Cells

Previous studies have demonstrated reduced levels of KCNMA1, which forms the α subunits of a Ca^{2+}-activated K^+ channel called the BK channel (Dworetzky et al., 1994; Langer et al., 2003), in cochlear HCs of $Tmprss3^{Y260X}$ mice (Molina et al., 2013). Since BK channels have also been documented in the vestibular HCs of mammals (Kong et al., 2005; Schweizer et al., 2009), we sought to

Figure 3. Normal Development of Inner Ear Organoids and Mechanotransduction Apparatus of Hair Cells in Both R1/E (WT) and *Tmprss3*KO-GFPKI (KO) Organoids

(A) Schematic diagram for generating a mESC line with *Tmprss3* knockout and GFP knockin (*Tmprss3*KO-GFPKI). The 2A-nGFP sequence was inserted into the second exon ("exon 2") after the start codon and expressed using the endogenous promoter and start codon of *Tmprss3*, thereby disrupting translation of any *Tmprss3* transcript variants.

(B) Gel electrophoresis of PCR products. Green arrows indicate the primers used for amplification of the inserted 2A-nGFP-pA cassette and homology arm regions.

(C) Chromatogram of the region around exon 2 of *Tmprss3* with the 2A-nGFP cassette.

(D–F) Pluripotency markers as indicated for KO cell line (passage number 23).

(G and H) Representative images of ECAD and PAX8 staining D8 aggregates. Arrowheads indicate the $ECAD^+PAX8^+$ otic-epibranchial placode domain.

(I and J) $SOX2^+$ and $PAX2^+$ otic prosensory vesicles in D14 aggregates.

(K and L) Otic vesicles in D21 organoids. $MYO7A^+$ hair cells (HCs) and $SOX2^+$ supporting cells are evident.

(M and N) $MYO7A^+$ HCs with F-ACTIN-based hair bundles (white hollow arrowhead) in D23 organoids.

(O) Bright-field image of an opened otic vesicle for the FM1-43fx uptake assay. Red dashed lines indicate the sensory epithelium.

(P and Q) FM1-43fx uptake via mechanotransduction channels (15-s incubation) in WT (P) and KO (Q) HCs (n = 5 otic vesicles from each of three independent experiments).

(R–U) Representative images of PCDH15 (R and S) and CDH23 (T and U) labeling of tip links in D23 hair bundles.

(C) to (N) show otic vesicles (n = 15–20) from three independent experiments. Scale bars, 100 μm (D–F), 50 μm (G–L), 10 μm (M, N, P, and Q), 500 μm (O), and 1 μm (R–U).

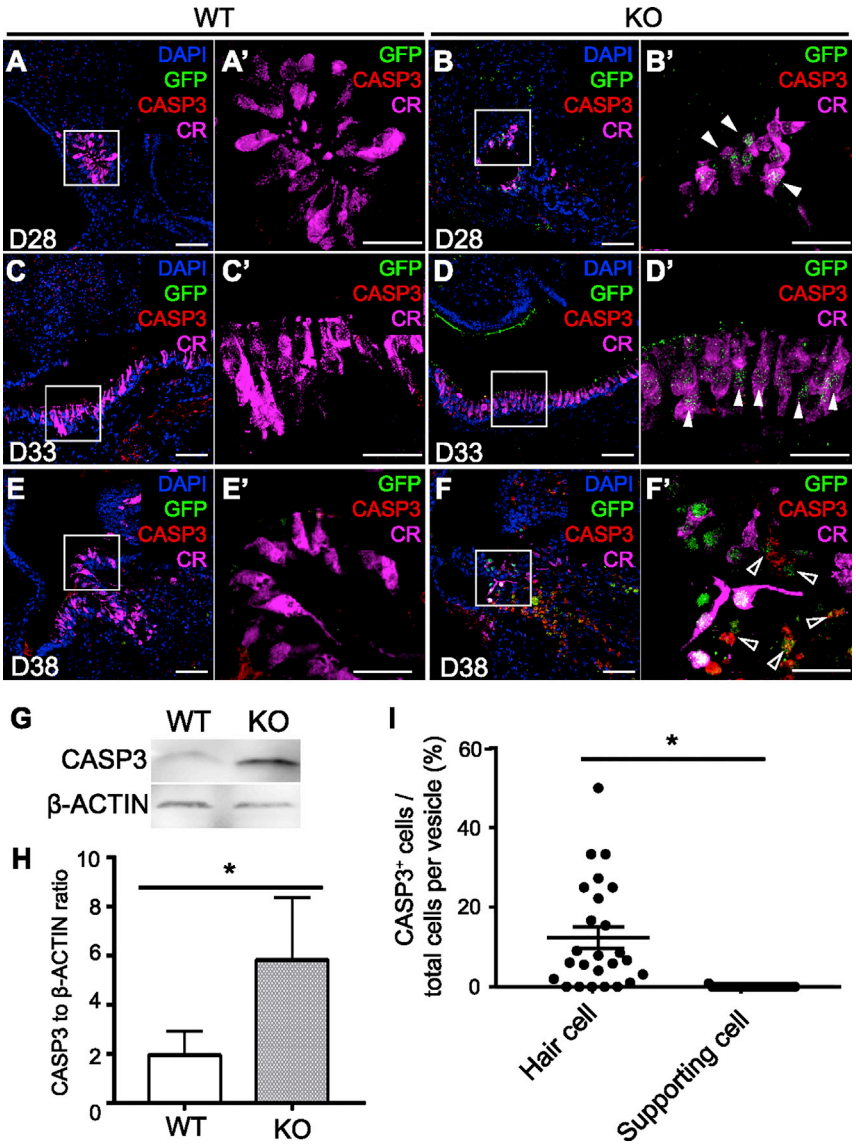

Figure 4. Increased Levels of Cleaved Caspase-3 in D38 *Tmprss3*KO-GFPKI (KO) Inner Ear Organoids

(A–F′) Representative images of R1/E (WT) and KO otic vesicles on various days. Hair cells (HC) labeled with the HC marker calretinin (CR). Magnified images of the areas enclosed within the white squares in (A) to (F) can be found in (A′) to (F′), respectively, and the white filled and hollow arrowheads indicate GFP$^+$ HCs and GFP$^+$CASP3$^+$ cells, respectively. Scale bars, 50 μm (A–F) and 25 μm (A′–F′).

(G and H) Western blot (G) and quantification (H) of CASP3 level (normalized to β-ACTIN) in D36 WT and KO organoids. Four experiments were performed and, in each experiment, random pools of 15–20 organoids were collected for protein extractions.

(I) Percentage of CASP3$^+$ HC and CASP3$^+$ SCs in D36 KO organoids. n = 25 KO otic vesicles from three independent experiments.

Error bars in graphs denote ±SEM; Student's t test, *p < 0.001. See also Figure S4.

document whether the lack of TMPRSS3 also reduces the abundance of BK channels in the HCs of inner ear organoids. To avoid the effects caused by apoptosis, rather than the lack of TMPRSS3, the levels of BK channels were compared in R1/E (WT) and *Tmprss3*KO-GFPKI (KO) organoids on D33. BK channels were detected in 66% of all HCs (marked by MYO7A and BRN3C staining) in WT otic vesicles (Figures 5A, 5B, and 5E), whereas a significantly lower percentage (~45%) was observed in D33 KO organoids ($p < 0.001$; Figures 5C–5E).

Gene Expression Profiles of Inner Ear Organoids in R1/E and *Tmprss3*KO-GFPKI

Next, to elucidate the molecular mechanisms underlying *Tmprss3* KO-caused HC degeneration, we carried out scRNA-seq. We profiled dissociated cells from R1/E (WT) and *Tmprss3*KO-GFPKI (KO) organoids at D25 and D35 using droplet microfluidics (10× Genomics Chromium) to obtain cell-barcoded cDNAs that were sequenced. We acquired high-quality reads from ~8,000–10,000 cells from both WT and KO across 10–12 inner ear organoids.

We performed unsupervised cell clustering using t-distributed stochastic neighbor embedding (tSNE). Putative HC clusters were established based on conventional HC markers, such as *TMC1*, *Myo7a*, *Pvalb*, and *Otof* (Figures 6A, 6C, and S5A–S5E). Expression of marker genes from neurons, oligodendrocytes, and epithelial cells was also observed in other clusters (Figure S5).

In both D25 WT and KO organoids, putative HC clusters constituted 2% of all cells (Figures S5A and S5B; Table S2).

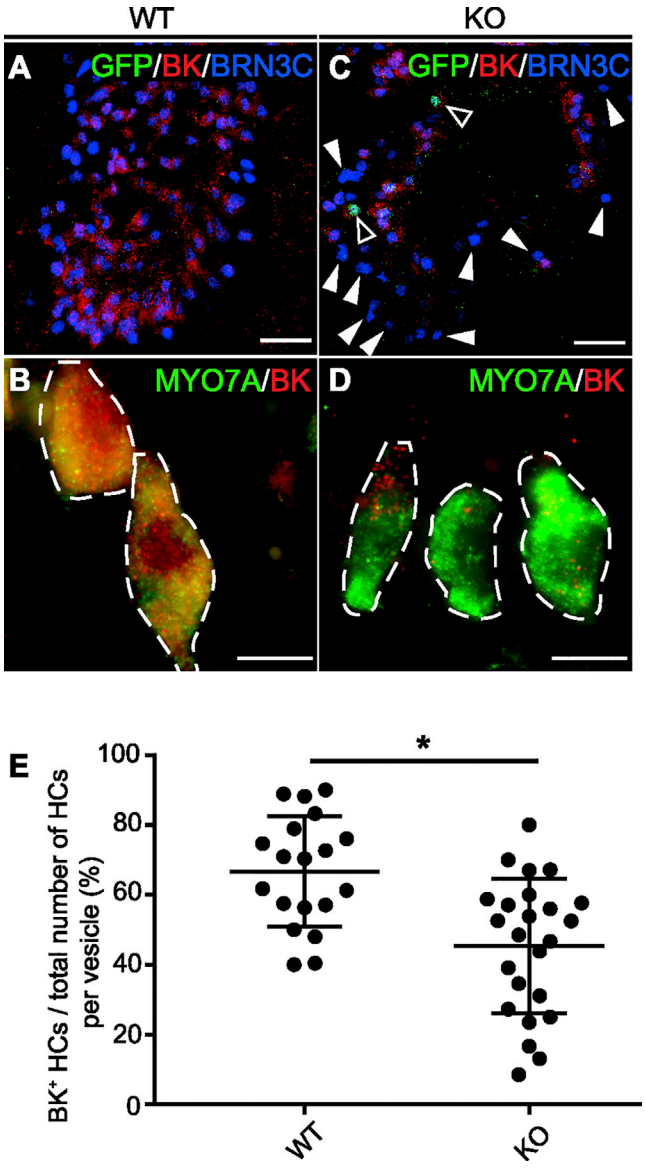

Figure 5. Decrease in Hair Cells with BK Channels in D33 *Tmprss3*KO-GFPKI (KO) Organoids

(A and B) Hair cells (HCs) displaying BK channels in R1/E (WT) organoids at D33. White dashed lines outline the HCs (B). Scale bar, 25 μm.

(C and D) Reduced number of HCs with BK channels in KO organoids at D33. The white filled and hollow arrowheads point to HC lacking BK channels and GFP$^+$ HC, respectively. White dashed lines outline the HCs (D). Scale bar, 25 μm.

(E) Dot plot of the percentage of HC with BK channels relative to the total number of HC in organoids (±SEM; n = 19 for WT otic vesicles and 24 for KO otic vesicles from three independent experiments; Student's t test, *p < 0.001).

Although the percentage of cells in the putative HC cluster decreased to 1.24% in D35 WT organoids, this percentage was nevertheless 2-fold higher than in the KO (0.67%) at this time (Table S2). Integrated comparative analyses of WT and KO were performed with D25 and D35 samples (Figures 6A, S5E, and S5F), and the ratio of KO/WT in the D35 HC cluster (0.58) was lower than for D25 (0.76). This finding is depicted graphically in Figure 6B and suggests that the HC number decreased at D35 in KO organoids as a result of *Tmprss3*-KO.

Statistically over-representation tests were performed using genes detected in putative HC clusters among the four samples. Although overall HC gene assembly did not differ between WT and KO samples from the same culture day, more genes involved in developmental processes were documented at the earlier sampling time (Table S3). We also observed more genes associated with mature HCs (e.g., *Kcna1*, *Calb2*, and *Tmc1* [Scheffer et al., 2015]) in D35 organoids. These data consequently shed light on inner ear organoid development.

To unravel the mechanisms underlying the HC degeneration that was observed in later cultures, we examined differences in average gene expression between D35 WT and D35 KO organoids (Figure 6D and Table S4). Less than 1% of all detected genes in the putative HC cluster were differentially expressed (41 differentially expressed genes [DEGs]; Table S4). There were 22 genes upregulated in the KO (KO-enriched) and 19 genes downregulated in the KO (KO-reduced). Integrated pathway analysis (IPA) of the KO-enriched genes linked to apoptosis while the KO-reduced genes did not link to a definitive pathway (Figures S5G and S5H). We also performed function clustering analyses on all DEGs, but no specific pathway or biological process was identified.

From protein-protein interaction analyses, we found that six DEGs (15%) were previously documented to interact with KCNMA1 in mouse cochlea (Kathiresan et al., 2009), and 16 DEGs (39%) encoding proteins interacting with 14-3-3-EPSILON (Figure 6D). Five of KO-reduced genes encode Ca^{2+}-binding proteins (Figure 6D). Also, a KO-reduced gene, Sln, encodes sarcolipin, which is a known Ca^{2+} regulator in muscle. On the other hand, 12 of the 22 KO-enriched genes encoded proteins that associated with the extracellular matrix (ECM) (Figure 6D). Taken together, our results suggest that loss of TMPRSS3 may influence intracellular Ca^{2+} homeostasis via its interaction with KCNMA1. Also, lack of TMPRSS3 might perturb the ECM in otic vesicles.

Cell Membrane Localization of TMPRSS3

To elucidate the subcellular localization of the TMPRSS3 protein, we constructed N-terminal-tagged 3×FLAG

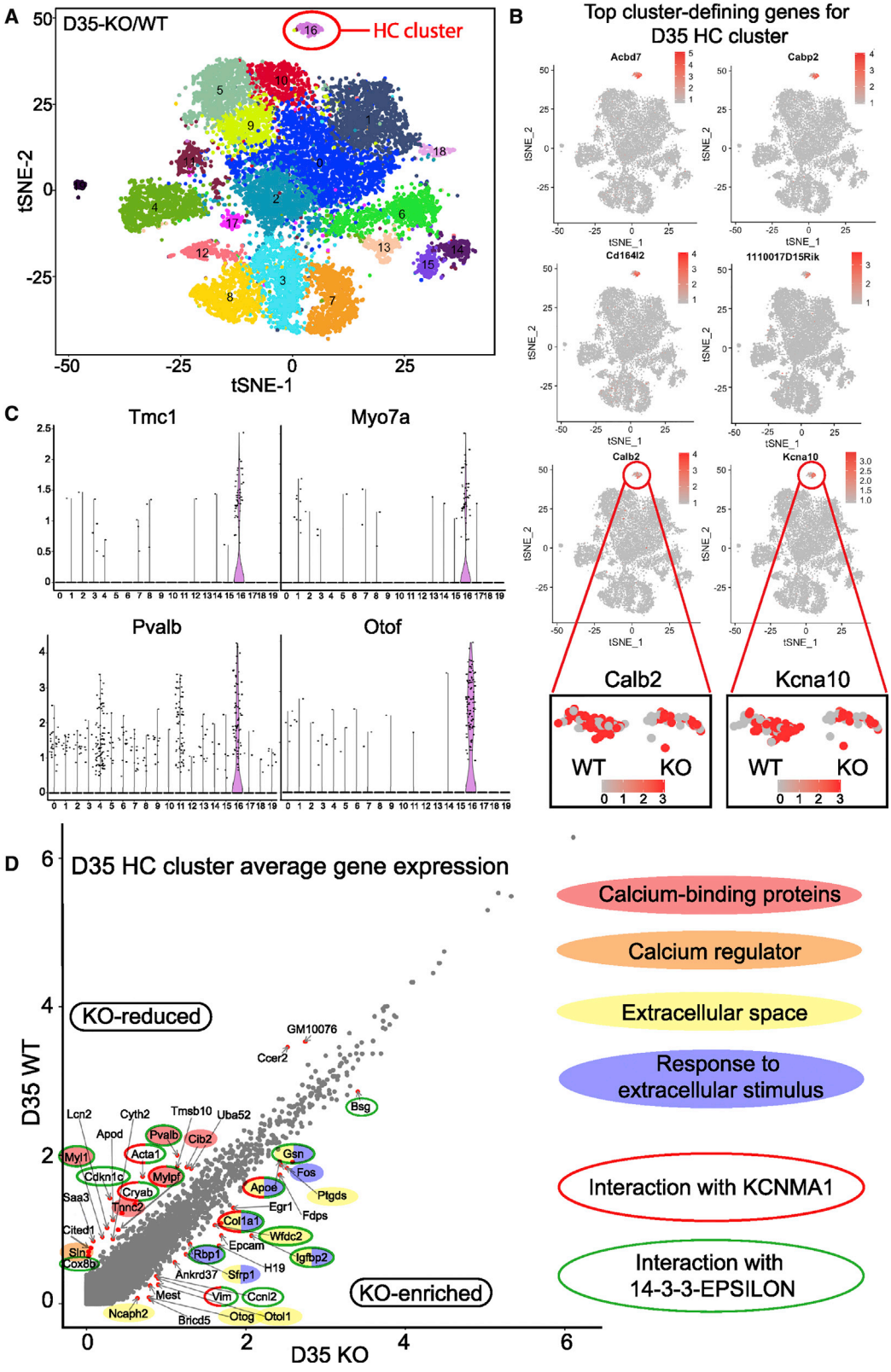

(legend on next page)

Tmprss3f, and knocked in the construct to the ROSA 26 locus of R1/E (Figures 7A and S6A–S6E); this caused 3×FLAG-*Tmprss3f* to be ubiquitously and constitutively expressed in all cells. Western blot with an anti-FLAG antibody presented a band at approximately 58–60 kDa in R1/E−3×FLAG-*Tmprss3f* samples but not in R1/E samples (Figure 7B). In addition, the FLAG antibody recognized a 28-kDa band (Figure 7B), which is similar in size to an N-terminal fragment of 28.6 kDa after autocleavage at the predicted serine protease catalytic site of TMPRSS3F (Lee et al., 2003; Wattenhofer et al., 2005).

During inner ear organoid induction, we noted non-nuclear staining corresponding to 3×FLAG-TMPRSS3F that was punctate and overlapping with E-cadherin (ECAD), both localized to the plasma membrane in D14 aggregates (Figures 7C–7D′). Subsequently, we attempted to determine the localization of 3×FLAG-TMPRSS3F in organoid HCs and found that it also labeled the cell membrane, as well as in the cytoplasm (Figure S6F). To improve resolution, we localized 3×FLAG-TMPRSS3F on a monolayer of 3×-FLAG-*Tmprss3f* ESCs, and further confirmed the localization on cell membranes via the co-localization of FLAG and phalloidin (F-ACTIN; Figure 7E). TMPRSS3 was previously reported to localize to the ER (Guipponi et al., 2008). Therefore, we examined whether 3×FLAG-TMPRSS3F localizes to the ER using the ER marker CALRETICULIN, and observed partially overlapping staining (Figure 7F). We also noticed dense staining in the cytoplasm, potentially in/on the Golgi apparatus. Staining of Golgi-97 with an anti-FLAG antibody revealed overlapped staining (Figure 7G). Quantitative co-localization analyses indicated a positive correlation (Pearson's correlation) and complete co-localization (Van Steensel's cross-correlation functions plots) between FLAG and F-ACTIN signals (Figure 7H). On the other hand, Pearson's correlation coefficient (r) values for FLAG versus ER and FLAG versus the Golgi apparatus were 0.306 and 0.364, respectively; however, as the values were less than 0.5, complete positive co-localization was inconclusive. Overall, we showed proteolytic active TMPRSS3 localized on the cell membrane using transgenic mESC and inner ear organoid systems.

DISCUSSION

Our findings demonstrate that inner ear organoids recapitulate the *in vivo* development and pathology of HCs seen in mice (*Tmprss3*^{Y260X}). FM1-43fx uptake assay, unlike electrophysiology that examines mechanotransduction function by deflecting HBs and measuring membrane potential changes, determines the existence of mechanotransduction apparatus based on the uptake of dye through channels within 10–15 s. The similar level of FM1-43fx uptake in both WT and *Tmprss3*-KO HCs, as well as the presence of intact tip link components, suggest that lack of TMPRSS3 does not impede the formation of the mechanotransduction apparatus as such, TMPRSS3 is not required for development nor early mechanotransduction, but rather is integral to HC survival.

We found increased CASP3 signals in both sensory epithelia of *Tmprss3*^{Y260X} and C3H-Y260, as well as in organoids completely lacking TMPRSS3. The elevation of CASP3 suggests that HC death is a consequence of apoptosis. The anatomical integrity of HCs lacking TMPRSS3 protease activity differed from that of cells lacking the protein in its entirety. In D38 *Tmprss3*KO-GFPKI organoids HCs were difficult to identify, whereas D38 C3H-Y260X2 otic vesicles featured distinguishable HCs in the sensory epithelia. This suggests a genotype-phenotype correlation, which supports previous findings based on human genetic and patient data in which the phenotypes of individuals with *Tmprss3* mutations vary widely according to genotype variants (Weegerink et al., 2011).

Loss of TMPRSS3-protease activity was previously reported to reduce cellular levels of KCNMA1 (the α subunits of the BK channel) in mouse cochlear HCs (Molina et al., 2013). In this study, we observed a significant decrease in BK channels in KO HCs. Additionally, the reduced expression of several genes encoding Ca^{2+}-binding proteins and intracellular Ca^{2+} regulators in D35 KO HCs via scRNA-seq analyses might be a response to altered Ca^{2+} homeostasis due to decreased BK channels. Furthermore, among D35 DEGs in the HC cluster, we identified six genes that encode proteins known to interact with KCNMA1 (Kathiresan et al., 2009). 14-3-3-EPSILON,

Figure 6. Comparison of Single-Cell Gene Expression Profiles between R1/E (WT) and *Tmprss*3KO-GFPKI (KO) Inner Ear Organoids

(A) tSNE plot of D35 WT and D35 KO organoids after integrated comparative analyses. The red circle indicates the putative hair cell (HC) cluster.

(B) Top six cluster-defining genes for the putative HC clusters. Specifically, Calb2 and Kcna10 are postnatal HC markers (Scheffer et al., 2015). Cells from D35 WT and D35 KO strongly expressing these markers contributing the putative HC cluster in (A) are shown.

(C) HC markers used to identify the putative HC cluster.

(D) Analyses of difference in average gene expressions in the putative HC cluster between D35 WT and D35 KO. Genes encoding Ca^{2+}-binding proteins (red), extracellular proteins (yellow), and proteins responding extracellular stimuli (blue) are indicated by color. Gene-encoding proteins interacting with KCNMA1 and protein EPSILON are circled by red and green, respectively.

See also Figure S5.

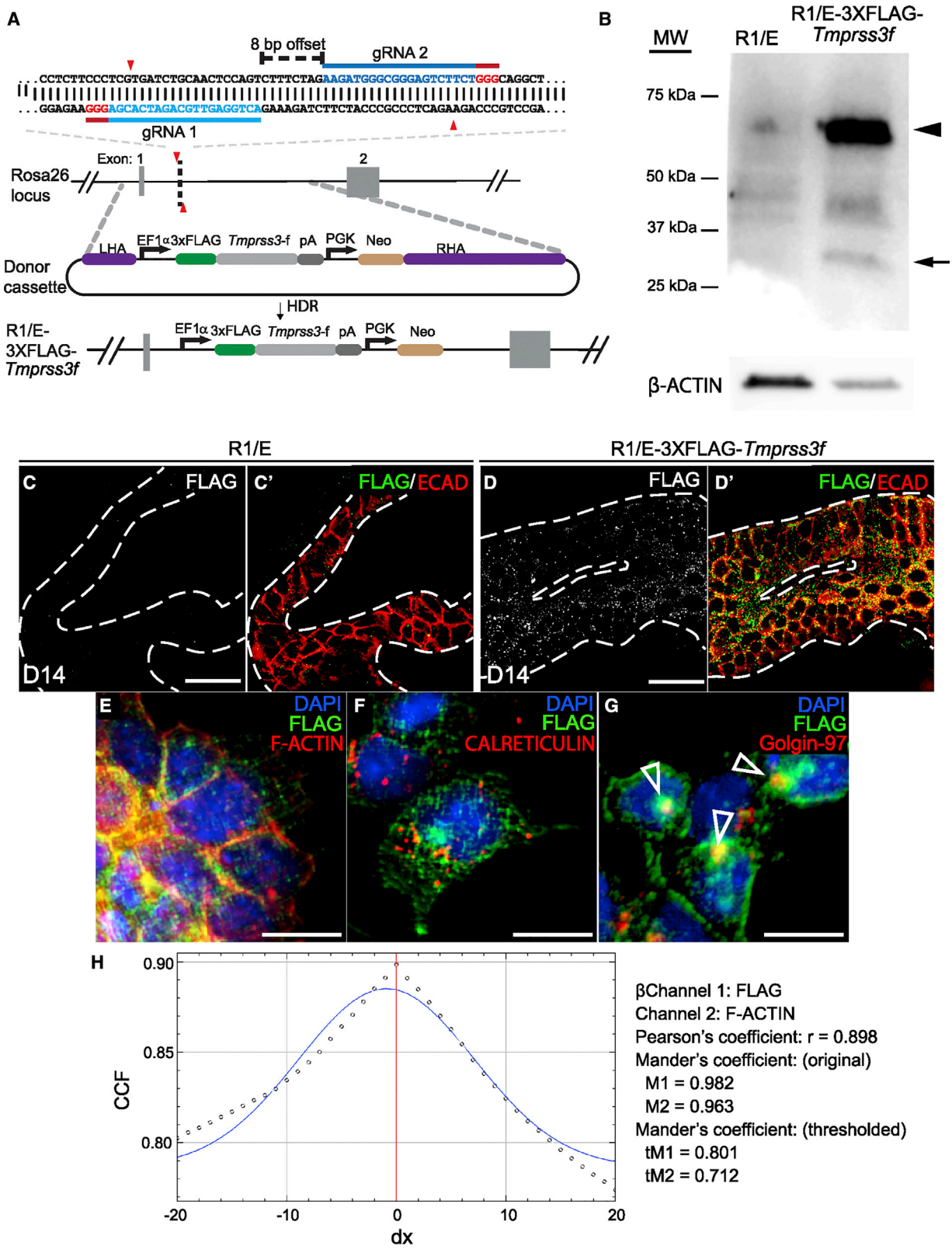

(legend on next page)

which was reported to interact with multiple DEGs via protein-protein interaction analyses, was also known to be the putative protein-binding partner with BK channels and to affect its expression (Sokolowski et al., 2011). Mice lacking 14-3-3 ETA (a family member of 14-3-3-EPSILON) exhibit cochlear HC degeneration via apoptosis (Buret et al., 2016). Previous studies have demonstrated that inhibition of BK channels can cause cell apoptosis (Bortner and Cidlowski, 2014; Sakai and Sokolowski, 2015). Although no biological pathways were significantly enriched upon analysis of the DEGs, genes involved in both apoptosis and cell survival were revealed after further exploring potential interactions using IPA (Figures S5G and S5H.). Based on these data, one possible mechanism of HC loss is that defective TMPRSS3 leads to a decrease in BK channels via interactions with KCNMA1 with subsequent disruptions in intracellular Ca^{2+} homeostasis, resulting thereafter in HC apoptosis.

Differential gene expression analyses also showed that more than half of genes enriched in D35 KO HCs encode proteins that either regulate or structurally comprise ECM; this finding could be linked to the subcellular localization of TMPRSS3 on the cell surface. Although TMPRSS3 was only reported at ER previously (Guipponi et al., 2002, 2008), it should be noted that cell membrane localization is more commonly reported for other members of the TMPRSS family (Brunati et al., 2015; Chen et al., 2010; Tsuji et al., 1991). According to our data from scRNA-seq and 3×FLAG-tagged TMPRSS3F we proposed that, in addition to effects on the Ca^{2+} homeostasis, TMPRSS3 might also play roles in organization or regulation of ECM. Indeed, other members of the TMPRSS family have been shown to undertake multiple cellular functions in different cellular locations (Böttcher-Friebertshäuser et al., 2010, 2013; Chen et al., 2010). Moreover, other yet to be identified protease substrates for TMPRSS3 are likely critical to the survival of HCs. For example, mutations in TMPRSS1 (also known as hepsin) also lead to hearing loss (Guipponi et al., 2007). Mutations in hepatocyte growth factor (HGF), which is regulated by TMPRSS1 (Hsu et al., 2012), cause deafness in humans (DFNB39) (Schultz et al., 2009). Future studies exploring a similar functional interaction and other protease substrates of TMPRSS3 in the inner ear are of consequent need.

There are current limitations of stem cell-derived inner ear organoids. First, upon further optimizing previously published protocols (Koehler et al., 2013; Koehler and Hashino, 2014), we extended the culture time from 30 to 45–50 days; however, organoid integrity became variable after D38, potentially due to the outgrowth of non-otic tissues. Therefore, D38 was chosen as the latest sampling time in this study to avoid any potential artifacts or degeneration arising from stress associated with long-term culture. Second, the protocol for inducing organoids varies across cell lines, and optimization for each cell line is necessary. Although both C3H- and R1/E-based lines gave rise to inner ear organoids after optimizing the protocol (Figure S7), the induction efficiency among cell lines remains significantly different (the induction efficiency of R1/E-based cell lines [85%] and C3H-based ones [49%]; t test, $p < 0.05$ [three 96-well plate experiments]).

In summary, using a TMPRSS3 mutant model we demonstrate that inner ear organoids are capable of recapitulating genetic-associated phenotypes observed *in vivo*. Furthermore, with transgenic cell lines and scRNA-seq analyses, we revealed that cell membrane-bound TMPRSS3 is an essential component for HC homeostasis and survival. The scRNA-seq data from D35 inner ear organoids, which are equivalent to P12–P14 mouse inner ears, provided insight into HC development and the cellular roles of TMPRSS3. This study not only provides data on the role of TMPRSS3 in inner ear HCs, but it also highlights the utility of organoid systems as a powerful tool for understanding the genetic underpinnings of mammalian disease.

Figure 7. Cell-Surface Localization of TMPRSS3

(A) Schematic diagram for generating a mESC featuring N-terminally tagged 3×FLAG-TMPRSS3.

(B) Representative western blot image of protein samples from D20 R1/E and R1/E-3×FLAG-*Tmprss3f* organoids. The arrowhead indicates the intact 3×FLAG-TMPRSS3F, and the arrow indicates the N-terminal portion of 3×FLAG-TMPRSS3F after autocleavage.

(C–D′) Immunohistochemistry (IHC) images of anti-FLAG and ECAD in D14 aggregates as indicated. White dashed lines indicate $ECAD^{+}$ epithelia.

(E) IHC image of anti-FLAG co-localized with F-ACTIN (phalloidin staining).

(F) IHC image revealing anti-FLAG and CALRETICULIN (ER marker) staining.

(G) IHC image depicting anti-FLAG and Golgi-97 staining. White arrowheads indicate regions of overlapping anti-FLAG and Golgi-97 staining.

(H) Co-localization analysis of anti-FLAG and F-ACTIN staining using JACoP in ImageJ; the Van Steensel's cross-correlation functions (CCF) plot suggested complete co-localization. Pearson's coefficient r value and Mander's coefficient values for anti-FLAG and phalloidin are included.

Scale bars, 25 μm (C–D′) and 10 μm (E–G). See also Figure S6.

EXPERIMENTAL PROCEDURES

Mouse Specimens

The care and use of animals were approved by the Indiana University School of Medicine's Institutional Animal Care and Use Committee. WT (C3HeB/FeJ; *Tmprss3*^{WT}) and *Tmprss3* mutant mice (*Tmprss3*^{Y260X}) were kind gifts from Dr. Michel Guipponi's laboratory.

Derivation of mESCs

Derivation of mESCs from *Tmprss3*^{WT} and *Tmprss3*^{Y260X} mice followed the protocol of Czechanski et al. (2014). See Supplemental Experimental Procedures for details.

Generation of the *Tmprss3*-KO ESC and 3×FLAG-Tagged *Tmprss3* Lines

A Cas9n vector containing two guide RNAs (offset = 4 bp; *Tmprss3*_g1 and _g2; Table S5) targeting the adjacent region to the start codon of *Tmprss3* was manufactured by DNA 2.0. The donor vector was assembled from a 2A-nGFP-PGK-Puro cassette, two ~1-kb homology arms (LHA and RHA), and a pUC19 backbone using the Gibson Assembly master mix (New England Biolabs). The two homology arms were amplified from R1/E (ATCC SCRC-1036) genomic DNA (*Tmprss3*_LHA and *Tmprss3*_RHA; Table S5). The Cas9n vector and the donor vector were transfected into R1/E mESCs following the manufacturer's protocol (P3 Primary Cell 4D-Nucleofector X kit, Lonza). The transfection was carried out in a 4D Nucleofector using the program CB-150. Cells then were maintained in modified LIF-2i medium (Table S6) (Choi et al., 2017) supplemented with 1 μM Scr7 (Xcessbio) for 48 h before puromycin selection as follows: medium containing 0.5 μg/mL puromycin was changed daily for 5 days before removing the PGK-Puro subcassette by transfecting a vector expressing Cre recombinase (Addgene #13775). Isolation of clonal cell lines followed a published protocol (Ran et al., 2013). Successful insertion of the 2A-nGFP cassette was verified by PCR followed by DNA sequencing. 3×FLAG-tagged *Tmprss3* mESC was generated in similar procedures. See Supplemental Experimental Procedures for details.

Induction of Inner Ear Organoids

Induction followed the protocol of Koehler and Hashino (2014), but with modifications (Figure S7). In brief, ESCs were dissociated in Accutase (STEMCELL Technologies) and resuspended in differentiation medium (DMLK; Table S6). On D0, 1,500 cells in 100 μL of DMLK per well were plated in low binding 96-well U-bottomed plates (Thermo Fisher). On D1, half of the medium was exchanged with fresh DMLK containing Matrigel (Corning; 2% final concentration). Bone morphogenetic protein 4 (PromoKine) and SB-431542 (Reprocell) were added on D3. Later, basic fibroblast growth factor (STEMCELL Technologies) and LDN-193189 (Reprocell) were added (Figure S7). On D8, aggregates were washed twice in PBS before being transferred to new 96-well U-bottomed plates in 100 μL of N2 medium (Table S6) containing 1% Matrigel and 3 μM CHIR99021 (DeJonge et al., 2016). After 48 h, aggregates were transferred to 24-well low binding plates in fresh N2 medium until D20. On D20, aggregates were cultured in organoid medium (Table S6) with constant shaking. Half of the medium was changed every other day during the long-term culture period.

scRNA-Seq of Inner Ear Organoids

Ten to twelve organoids were dissociated in TrypLE Express (Thermo Fisher) at 37°C with shaking for 40 min. During dissociation, samples were mixed with pipetting every 5–10 min. Dissociated cells were filtered through a 40-μm cell strainer (Flowmi) followed by three washes with Dulbecco's PBS + 2% BSA. Single-cell 3′ RNA-seq experiments were conducted using the Chromium single-cell system (10x Genomics) and Illumina sequencers at the Center for Medical Genetics of Indiana University School of Medicine. See Supplemental Experimental Procedures for the scRNA-seq data process.

Analysis of scRNA-Seq Data

Integrated comparative analyses of two scRNA datasets were performed using Seurat 2.3 (Butler et al., 2018). In brief, Seurat objects were set up and genes that were used in the analyses were chosen. Canonical correlation analyses (CCA) were carried out and alignments of CCA subspaces were performed to generate a new dimension reduction. Clusters for the new dimension reduction of integrated analyses were visualized using tSNE plots. Annotations of clusters (Figures S5A–S5D) were determined using top cluster-defining genes in addition to the data annotation based on mouse RNA-seq samples using the package singleR (Aran et al., 2018). Average gene expressions were compared between samples (WT versus KO) within the same cluster. Scatterplots showed average gene expression comparisons, and genes enriched in samples were indicated.

Gene ontology analyses were performed with annotation tools, Panther v14 (Mi et al., 2019) and STRING v11.0 (Gable et al., 2018). Protein-protein interaction analysis was conducted using IntAct (https://www.ebi.ac.uk/intact/). Protein-protein interactions including at least three DEGs are presented in the main text. Gene over-representation tests, which examined whether biological processes and molecular features are enriched in the gene list of the HC cluster between samples, were carried out in Panther v14.

Microscopic Imaging and Statistical Analyses

See Supplemental Experimental Procedures for immunohistochemistry procedures. For assessment of the concentration of the apoptotic marker CASP3 in mouse vestibular sensory epithelia and C3H-derived otic vesicles, fluorescence intensity was measured (as gray values) from raw images using ImageJ software (NIH). For each vestibular sensory epithelium, gray values were averaged from three to four sections across the tissue. Six sensory epithelia for each vestibular organ type were included in the statistical analyses. Otic vesicles were identified based on the presence of HCs enclosed in the circular structure formed by SOX2^{+} cells (Figure S3). Gray values from three to five sections of one otic vesicle were averaged, and 14–16 otic vesicles from three independent experiments were included in statistical analyses. One-tailed t tests were carried out between WT and *Tmprss3* mutant samples, and it was hypothesized that the latter would be characterized by higher CASP3 levels; an α level of 0.05 was set a priori.

Counting of CASP3$^+$MYO7A$^+$ HCs, CASP3$^+$SOX2$^+$MYO7A$^-$ SCs, and BK$^+$BRN3C$^+$ HCs was carried out with ImageJ. Data ($n \geq 19$ otic vesicles; see details in figure legends.) were collected from at least three different experiments. Two-tailed t tests ($p < 0.05$) were used to uncover differences in CASP3$^+$ cells between cell types. Student's t tests were carried out to compare the percentage of HCs expressing BK channels relative to the total number of HCs in otic vesicles between R1/E and *Tmprss3*-KO organoids. All statistical analyses were conducted with GraphPad Prism7.

ACCESSION NUMBERS

The accession number for the raw data files of RNA-seq analyses reported in this paper is GEO: GSE130649.

SUPPLEMENTAL INFORMATION

Supplemental Information can be found online at https://doi.org/10.1016/j.stemcr.2019.05.014.

AUTHOR CONTRIBUTIONS

P.-C.T. contributed to the design of the study, performed experiments, collected, analyzed, and interpreted data, and wrote the manuscript. A.L.A., J.N., and J.L. assisted with experiments. K.T.B. performed IPA analysis. A.A.R. helped with the design of experiments. R.F.N. conceived and supervised the study. E.H. and K.R.K. contributed to the design of experiments. Most authors reviewed the manuscript, and all approved the final version.

ACKNOWLEDGMENTS

We thank the IUSM Genomics Core (X. Xuei, H. Gao, and P. McGuire) for performing scRNA-seq and bioinformatics analyses, H. Chen for collecting mouse embryos, A.B. Mayfield for reviewing the manuscript, R. Smith for reviewing scRNA-seq data, and E. Longworth-Mills for assistance in the laboratory procedures. This work was supported by the National Institutes of Health (K08-DC016034 to R.F.N., R01-DC015788 to E.H., and R03-DC015624 to K.R.K.), the Triological Society and American College of Surgeons (Clinician Scientist Development Award to R.F.N.), the American Academy of Otolaryngology—Head & Neck Surgery (award 351873 to R.F.N.), the Ralph W. and Grace M. Showalter Research Trust (to R.F.N.), and the Department of Otolaryngology—HNS at Indiana University.

Received: December 6, 2018
Revised: May 14, 2019
Accepted: May 15, 2019
Published: June 13, 2019

REFERENCES

Aran, D., Looney, A.P., Liu, L., Fong, V., Hsu, A., Wolters, P.J., Abate, A., Butte, A.J., and Bhattacharya, M. (2018). Reference-based annotation of single-cell transcriptomes identifies a profibrotic macrophage niche after tissue injury. BioRxiv https://doi.org/10.1101/284604.

Bademci, G., Foster, J., 2nd, Mahdieh, N., Bonyadi, M., Duman, D., Cengiz, F.B., Menendez, I., Diaz-Horta, O., Shirkavand, A., Zeinali, S., et al. (2016). Comprehensive analysis via exome sequencing uncovers genetic etiology in autosomal recessive nonsyndromic deafness in a large multiethnic cohort. Genet. Med. *18*, 364–371.

Barre, O., Dufour, A., Eckhard, U., Kappelhoff, R., Beliveau, F., Leduc, R., and Overall, C.M. (2014). Cleavage specificity analysis of six type II transmembrane serine proteases (TTSPs) using PICS with proteome-derived peptide libraries. PLoS One *9*, e105984.

Bortner, C.D., and Cidlowski, J.A. (2014). Ion channels and apoptosis in cancer. Philos. Trans. R. Soc. Lond. B, Biol. Sci. *369*, 20130104.

Böttcher-Friebertshäuser, E., Freuer, C., Sielaff, F., Schmidt, S., Eickmann, M., Uhlendorff, J., Steinmetzer, T., Klenk, H.-D., and Garten, W. (2010). Cleavage of influenza virus hemagglutinin by airway proteases TMPRSS2 and HAT differs in subcellular localization and susceptibility to protease inhibitors. J. Virol. *84*, 5605–5614.

Böttcher-Friebertshäuser, E., Klenk, H.-D., and Garten, W. (2013). Activation of influenza viruses by proteases from host cells and bacteria in the human airway epithelium. Pathog. Dis. *69*, 87–100.

Brunati, M., Perucca, S., Han, L., Cattaneo, A., Consolato, F., Andolfo, A., Schaeffer, C., Olinger, E., Peng, J., Santambrogio, S., et al. (2015). The serine protease hepsin mediates urinary secretion and polymerisation of Zona Pellucida domain protein uromodulin. Elife *4*, e08887.

Buret, L., Rebillard, G., Brun, E., Angebault, C., Pequignot, M., Lenoir, M., Do-Cruzeiro, M., Tournier, E., Cornille, K., Saleur, A., et al. (2016). Loss of function of Ywhah in mice induces deafness and cochlear outer hair cells' degeneration. Cell Death Dis. *2*, 16017.

Butler, A., Hoffman, P., Smibert, P., Papalexi, E., and Satija, R. (2018). Integrating single-cell transcriptomic data across different conditions, technologies, and species. Nat. Biotechnol. *36*, 411–420.

Chen, Y.-W., Lee, M.-S., Lee, M.-S., Lucht, A., Chou, F.-P., Huang, W., Havighurst, T.C., Kim, K., Wang, J.-K., Antalis, T.M., et al. (2010). TMPRSS2, a serine protease expressed in the prostate on the apical surface of luminal epithelial cells and released into semen in prostasomes, is misregulated in prostate cancer cells. Am. J. Pathol. *176*, 2986–2996.

Choi, J., Huebner, A.J., Clement, K., Walsh, R.M., Savol, A., Lin, K., Gu, H., Di Stefano, B., Brumbaugh, J., Kim, S.-Y., et al. (2017). Prolonged Mek1/2 suppression impairs the developmental potential of embryonic stem cells. Nature *548*, 219–223.

Czechanski, A., Byers, C., Greenstein, I., Schrode, N., Donahue, L.R., Hadjantonakis, A.K., and Reinholdt, L.G. (2014). Derivation and characterization of mouse embryonic stem cells from permissive and nonpermissive strains. Nat. Protoc. *9*, 559–574.

DeJonge, R.E., Liu, X.P., Deig, C.R., Heller, S., Koehler, K.R., and Hashino, E. (2016). Modulation of Wnt signaling enhances inner ear organoid development in 3D culture. PLoS One *11*, e0162508.

Dworetzky, S.I., Trojnacki, J.T., and Gribkoff, V.K. (1994). Cloning and expression of a human large-conductance calcium-activated potassium channel. Brain Res. Mol. Brain Res. *27*, 189–193.

Fasquelle, L., Scott, H.S., Lenoir, M., Wang, J., Rebillard, G., Gaboyard, S., Venteo, S., Francois, F., Mausset-Bonnefont, A.L., Antonarakis, S.E., et al. (2011). Tmprss3, a transmembrane serine protease deficient in human DFNB8/10 deafness, is critical for cochlear hair cell survival at the onset of hearing. J. Biol. Chem. *286*, 17383–17397.

Fritzsch, B., and Straka, H. (2014). Evolution of vertebrate mechanosensory hair cells and inner ears: toward identifying stimuli that select mutation driven altered morphologies. J. Comp. Physiol. A. Neuroethol. Sens. Neural Behav. Physiol. *200*, 5–18.

Gable, A.L., Szklarczyk, D., Lyon, D., Simonovic, M., Wyder, S., Mering, C.V., Junge, A., Jensen, L.J., Doncheva, N.T., Huerta-Cepas, J., et al. (2018). STRING v11: protein–protein association networks with increased coverage, supporting functional discovery in genome-wide experimental datasets. Nucleic Acids Res. *47*, D607–D613.

Gillespie, P.G., and Muller, U. (2009). Mechanotransduction by hair cells: models, molecules, and mechanisms. Cell *139*, 33–44.

Guipponi, M., Tan, J., Cannon, P.Z., Donley, L., Crewther, P., Clarke, M., Wu, Q., Shepherd, R.K., and Scott, H.S. (2007). Mice deficient for the type II transmembrane serine protease, TMPRSS1/hepsin, exhibit profound hearing loss. Am. J. Pathol. *171*, 608–616.

Guipponi, M., Toh, M.-Y., Tan, J., Park, D., Hanson, K., Ballana, E., Kwong, D., Cannon, P.Z.F., Wu, Q., Gout, A., et al. (2008). An integrated genetic and functional analysis of the role of type II transmembrane serine proteases (TMPRSSs) in hearing loss. Hum. Mutat. *29*, 130–141.

Guipponi, M., Vuagniaux, G., Wattenhofer, M., Shibuya, K., Vazquez, M., Dougherty, L., Scamuffa, N., Guida, E., Okui, M., Rossier, C., et al. (2002). The transmembrane serine protease (TMPRSS3) mutated in deafness DFNB8/10 activates the epithelial sodium channel (ENaC) in vitro. Hum. Mol. Genet. *11*, 2829–2836.

Hsu, Y.C., Huang, H.P., Yu, I.S., Su, K.Y., Lin, S.R., Lin, W.C., Wu, H.L., Shi, G.Y., Tao, M.H., Kao, C.H., et al. (2012). Serine protease hepsin regulates hepatocyte size and hemodynamic retention of tumor cells by hepatocyte growth factor signaling in mice. Hepatology *56*, 1913–1923.

Kathiresan, T., Harvey, M., Orchard, S., Sakai, Y., and Sokolowski, B. (2009). A protein interaction network for the large conductance Ca^{2+}-activated K^{+} channel in the mouse cochlea. Mol. Cell Proteomics *8*, 1972–1987.

Kazmierczak, P., Sakaguchi, H., Tokita, J., Wilson-Kubalek, E.M., Milligan, R.A., Muller, U., and Kachar, B. (2007). Cadherin 23 and protocadherin 15 interact to form tip-link filaments in sensory hair cells. Nature *449*, 87–91.

Keats, B.J., and Corey, D.P. (1999). The usher syndromes. Am. J. Med. Genet. *89*, 158–166.

Koehler, K.R., and Hashino, E. (2014). 3D mouse embryonic stem cell culture for generating inner ear organoids. Nat. Protoc. *9*, 1229–1244.

Koehler, K.R., Mikosz, A.M., Molosh, A.I., Patel, D., and Hashino, E. (2013). Generation of inner ear sensory epithelia from pluripotent stem cells in 3D culture. Nature *500*, 217–221.

Kong, W.-J., Guo, C.-K., Zhang, S., Hao, J., Wang, Y.-j., and Li, Z.-W. (2005). The properties of ACh-induced BK currents in Guinea pig type II vestibular hair cells. Hear Res. *209*, 1–9.

Langer, P., Grunder, S., and Rusch, A. (2003). Expression of Ca^{2+}-activated BK channel mRNA and its splice variants in the rat cochlea. J. Comp. Neurol. *455*, 198–209.

Lee, Y.J., Park, D., Kim, S.Y., and Park, W.J. (2003). Pathogenic mutations but not polymorphisms in congenital and childhood onset autosomal recessive deafness disrupt the proteolytic activity of TMPRSS3. J. Med. Genet. *40*, 629–631.

Liu, X.P., Koehler, K.R., Mikosz, A.M., Hashino, E., and Holt, J.R. (2016). Functional development of mechanosensitive hair cells in stem cell-derived organoids parallels native vestibular hair cells. Nat. Commun. *7*, 11508.

Mak, A.C., Szeto, I.Y., Fritzsch, B., and Cheah, K.S. (2009). Differential and overlapping expression pattern of SOX2 and SOX9 in inner ear development. Gene Expr. Patterns *9*, 444–453.

Mi, H., Muruganujan, A., Huang, X., Ebert, D., Mills, C., Guo, X., and Thomas, P.D. (2019). Protocol update for large-scale genome and gene function analysis with the PANTHER classification system (v.14.0). Nat. Protoc. *14*, 703–721.

Molina, L., Fasquelle, L., Nouvian, R., Salvetat, N., Scott, H.S., Guipponi, M., Molina, F., Puel, J.L., and Delprat, B. (2013). Tmprss3 loss of function impairs cochlear inner hair cell Kcnma1 channel membrane expression. Hum. Mol. Genet. *22*, 1289–1299.

Oesterle, E.C., Campbell, S., Taylor, R.R., Forge, A., and Hume, C.R. (2008). Sox2 and JAGGED1 expression in normal and drug-damaged adult mouse inner ear. J. Assoc. Res. Otolaryngol. *9*, 65–89.

Peters, T.A., Levtchenko, E., Cremers, C.W., Curfs, J.H., and Monnens, L.A. (2006). No evidence of hearing loss in pseudohypoaldosteronism type 1 patients. Acta Otolaryngol. *126*, 237–239.

Ran, F.A., Hsu, P.D., Wright, J., Agarwala, V., Scott, D.A., and Zhang, F. (2013). Genome engineering using the CRISPR-Cas9 system. Nat. Protoc. *8*, 2281.

Sakai, Y., and Sokolowski, B. (2015). The large conductance calcium-activated potassium channel affects extrinsic and intrinsic mechanisms of apoptosis. J. Neurosci. Res. *93*, 745–754.

Scheffer, D.I., Shen, J., Corey, D.P., and Chen, Z.-Y. (2015). Gene expression by mouse inner ear hair cells during development. J. Neurosci. *35*, 6366–6380.

Schultz, J.M., Khan, S.N., Ahmed, Z.M., Riazuddin, S., Waryah, A.M., Chhatre, D., Starost, M.F., Ploplis, B., Buckley, S., Velasquez, D., et al. (2009). Noncoding mutations of HGF are associated with nonsyndromic hearing loss, DFNB39. Am. J. Hum. Genet. *85*, 25–39.

Schweizer, F.E., Savin, D., Luu, C., Sultemeier, D.R., and Hoffman, L.F. (2009). Distribution of high-conductance calcium-activated potassium channels in rat vestibular epithelia. J. Comp. Neurol. *517*, 134–145.

Scott, H.S., Kudoh, J., Wattenhofer, M., Shibuya, K., Berry, A., Chrast, R., Guipponi, M., Wang, J., Kawasaki, K., Asakawa, S., et al. (2001). Insertion of beta-satellite repeats identifies a transmembrane protease causing both congenital and childhood onset autosomal recessive deafness. Nat. Genet. *27*, 59–63.

Shinjo, Y., Jin, Y., and Kaga, K. (2007). Assessment of vestibular function of infants and children with congenital and acquired deafness using the ice-water caloric test, rotational chair test and vestibular-evoked myogenic potential recording. Acta Oto Laryngol. *127*, 736–747.

Siemens, J., Lillo, C., Dumont, R.A., Reynolds, A., Williams, D.S., Gillespie, P.G., and Muller, U. (2004). Cadherin 23 is a component of the tip link in hair-cell stereocilia. Nature *428*, 950–955.

Sloan-Heggen, C.M., Bierer, A.O., Shearer, A.E., Kolbe, D.L., Nishimura, C.J., Frees, K.L., Ephraim, S.S., Shibata, S.B., Booth, K.T., Campbell, C.A., et al. (2016). Comprehensive genetic testing in the clinical evaluation of 1119 patients with hearing loss. Hum. Genet. *135*, 441–450.

Sokolowski, B., Orchard, S., Harvey, M., Sridhar, S., and Sakai, Y. (2011). Conserved BK channel-protein interactions reveal signals relevant to cell death and survival. PLoS One *6*, e28532.

Szabo, R., and Bugge, T.H. (2011). Membrane-anchored serine proteases in vertebrate cell and developmental biology. Annu. Rev. Cell Dev. Biol. *27*, 213–235.

Tsuji, A., Torres-Rosado, A., Arai, T., Le Beau, M.M., Lemons, R.S., Chou, S.H., and Kurachi, K. (1991). Hepsin, a cell membrane-associated protease. Characterization, tissue distribution, and gene localization. J. Biol. Chem. *266*, 16948–16953.

Wattenhofer, M., Sahin-Calapoglu, N., Andreasen, D., Kalay, E., Caylan, R., Braillard, B., Fowler-Jaeger, N., Reymond, A., Rossier, B.C., Karaguzel, A., et al. (2005). A novel TMPRSS3 missense mutation in a DFNB8/10 family prevents proteolytic activation of the protein. Hum. Genet. *117*, 528–535.

Weegerink, N.J.D., Schraders, M., Oostrik, J., Huygen, P.L.M., Strom, T.M., Granneman, S., Pennings, R.J.E., Venselaar, H., Hoefsloot, L.H., Elting, M., et al. (2011). Genotype-phenotype correlation in DFNB8/10 families with TMPRSS3 mutations. J. Assoc. Res. Otolaryngol. *12*, 753–766.

Zhou, G., Kenna, M.A., Stevens, K., and Licameli, G. (2009). Assessment of saccular function in children with sensorineural hearing loss. Arch. Otolaryngol. Head Neck Surg. *135*, 40–44.